Planetary impacts: scaling of crater depth from subsonic to supersonic conditions

L. Allibert[1], M. Landeau[2], R. Röhlen[1], A. Maller[2], M. Nakajima[3]and K. Wünnemann[1]

[1]Museum für Naturkunde, Invalidenstrasse 43, Berlin, Germany

[2]Institut de Physique du Globe de Paris, Université Paris Cité, 1 Rue Jussieu, Paris, France

[3]University of Rochester, Department of Earth and Environmental Sciences, Rochester, NY, United States

Key Points:

- The shock physics code iSALE is successfully benchmarked against subsonic water impact experiments.
- A scaling law is proposed for the crater depth as a function of the Mach and Froude numbers which are varied as independent parameters.
- In the limit of high Mach numbers, our scaling suggests that the maximum crater depth is controlled by the sound velocity and gravity, but not by the impact speed.

Corresponding author: Laetitia Allibert, `laetitia.allibert@mfn.berlin`

Abstract

Planetary impacts have shaped the surfaces and interiors of planets. They were particularly decisive in the last stage of planetary accretion, as they have eventually formed terrestrial planets. During these large supersonic collisions, shock waves melted the impactor and the target, and formed silicate magma oceans. Because the propagation of shock waves and the melting is faster than the excavation of an impact crater, the cratering stage can be considered as a purely hydrodynamic process. Here, we use both laboratory impact experiments in water and numerical simulations to investigate the crater dimensions resulting from the impact of a liquid impactor onto a liquid target. We show that our numerical models reproduce the laboratory experiments at subsonic impact velocities. We then explore the effect of both the Froude number, which is the ratio of the impactor kinetic energy to gravity, and the Mach number, which is the ratio of the impact speed to the sound speed. We vary these two parameters independently in impact simulations, going from subsonic to supersonic conditions. We obtain a new scaling law for the crater dimension that describes the transition from subsonic to supersonic impacts. Our results indicate that the transition between these two regimes results from a change in the partitioning of the impactor kinetic energy into potential energy in the crater and internal energy. Finally, our scaling suggests that, in the limit of large Mach numbers, the crater depth depends only on the sound velocity and gravity, and is independent of the impact speed.

Plain Language Summary

Planetary formation involved a large number of very energetic collisions Such impacts generated shock waves which led to widespread melting and the formation of magma oceans. Understanding the dynamics of impacts into magma oceans is of great importance as these collisions set the initial temperature and composition of terrestrial planets and satellites. Laboratory experiments and numerical simulations have been used to investigate large impacts. However, each approach has pros and cons. Liquid impact experiments can produce the small scales responsible for the mixing between the impactor and the target, but they fail to reproduce shock waves and supersonic speeds. In contrast, current numerical simulations reach supersonic conditions but produce a limited amount of turbulence and mixing. In this study, we bridge the gap between these two methods and improve our understanding of the effect of the impact velocity on the cra-

tering process. Using the code iSALE, we numerically reproduce water impact experiments at low subsonic velocities. We then explore supersonic conditions in impact simulations. We obtain a new scaling law that predicts the crater depth in realistic impact conditions and better constrains the transition regime from subsonic to supersonic impacts.

1 Introduction

1.1 Motivation

Terrestrial planets experienced multiple large collisions during their formation (Chambers, 2004; Raymond et al., 2009; Walsh et al., 2011). During these energetic events, the shock compression caused substantial melting of the target and the impactor, generating magma ponds or global magma oceans (Tonks & Melosh, 1993; Elkins-Tanton, 2012; Nakajima et al., 2021; Manske et al., 2021). These large impacts events are though to have had important implications for the subsequent long-term thermochemical evolution of planets, and eventually played a role on the dynamo evolution (e.g. Monteux & Arkani-Hamed, 2014; O'Rourke & Stevenson, 2016; Badro et al., 2016).

Besides impact-induced heating of the planetary interior, understanding the dynamics of large collisions is also important for the chemical composition of the core and mantle of terrestrial planets. With each collision, the liquid core of the impactor breaks apart, the fragments sink in the magma ocean, and eventually merge with the core of the planet. During its traverse through the magma ocean, liquid metal mixes, and hence equilibrates chemically, with liquid silicates (e.g., Rubie et al., 2003). The composition of metal and silicates after this equilibration depends on pressure, temperature and redox conditions but also on the mixing of metal and silicates upon impact (e.g., Rubie et al., 2003).

Previous studies on the sedimentation of iron drops in a magma ocean showed that efficient equilibration requires mixing down to small spatial scales on the order of 1cm (e.g., Ichikawa et al., 2010; Ulvrová et al., 2011; Samuel, 2012; Qaddah et al., 2019). Such scales are usually much smaller than the spatial resolution in numerical impact simulations . In contrast, laboratory impact experiments using liquids can produce the small scales responsible for turbulent mixing. In addition, considering the large energy involved in planetary impacts, water-like fluid target material and magma oceans are thought to

show comparable impact dynamics. Experiments have been used to quantify the mixing between metal and silicates during and after a large impact (e.g., Deguen et al., 2014; Lherm & Deguen, 2018; Landeau et al., 2021; Lherm et al., 2022). However, in existing experiments the velocity is limited to a few meters per second, which is more than two orders of magnitude smaller than the sound speed. Thus, the hypervelocity reached by natural impacts and the generation of shock waves cannot be addressed in such experiments. Yet, it is well known that supersonic velocities and shock waves control the excavation of the crater (e.g., Melosh, 1989), which itself affects metal-silicate mixing (Kendall & Melosh, 2016; Lherm et al., 2022). In this study, we aim at investigating the effect of supersonic velocities and shock waves on impact cratering in a magma ocean. This is an important preliminary step towards ultimately extrapolating to supersonic conditions the mixing and the equilibration predicted by subsonic experiments to the supersonic regime. .

However, the transition from subsonic to hypervelocity liquid impacts , and its effect on cratering, have not been fully explored. During cratering, the maximum crater size depends on the Froude number Fr, which is the ratio of inertia to gravity forces, defined as $Fr = U^2/(gR)$, where R is the impactor radius (all variables are given in SI units) (Melosh, 1989). K. Holsapple and Schmidt (1982) showed that the scaling laws for the crater size obtained from hypervelocity impacts pass through the data for subsonic water-drop experiments. This successful extrapolation over six orders of magnitude in Froude number is remarkable, however not well understood, in particular due to the fact that no data exist in between the two regimes. The shock waves generated by hypervelocity impacts drastically affect the mechanism of crater formation. It is therefore unexpected that scaling laws for supersonic impacts agree with results from subsonic impacts. More importantly, previous scalings ignore the independent effect of the Mach number M, which is the ratio of the impact speed to the sound speed, in addition to the Froude number. This requires in depth investigation.

1.2 Scaling of crater size in liquids

Impact processes have shaped the solar system so profoundly that almost all images of planetary bodies show landscapes peppered with crater structures. Studies have used impact simulations and laboratory experiments to understand these impact processes (e.g., Gault et al., 1974; Schmidt, 1977; K. Holsapple & Schmidt, 1980; Melosh,

1989; K. R. Housen & Holsapple, 2003; Güldemeister et al., 2015; K. R. Housen et al., 2018; Landeau et al., 2021). Previous scaling laws link the properties of an impact crater, such as its depth and diameter, to the impact velocity, the impactor size and the material properties (e.g., K. Holsapple & Schmidt, 1982; K. A. Holsapple, 1993; Elbeshausen et al., 2009; K. R. Housen & Holsapple, 2011). The objective of these scaling laws is to deduce the conditions of impact from a given observable crater, or vice versa, to predict the shape of a crater that a certain impactor at a given velocity would produce. The subject has received much attention over the years. Different impact conditions (material, speed, angle) and outcomes (crater depth, crater radius, crater volume) have been studied. A variety of dimensionless numbers involving impact parameters have been introduced and linked to various outcomes (see K. Holsapple & Schmidt, 1982, for a review) from the crater shape and size (e.g., K. R. Housen & Holsapple, 2003) to the ejecta layering produced around the crater (e.g., K. Housen et al., 1983; K. R. Housen & Holsapple, 2011; Hyodo & Genda, 2020). In the planetary impact community, the π-group scaling is generally used (e.g., K. Holsapple & Schmidt, 1982; Melosh, 1989). This formalism describes the crater morphometry using dimensionless ratios corresponding to geometric parameters: the crater efficiency, defined as $\pi_v = \rho V/m$, but also $\pi_D = D(\rho/m)^{1/3}$ for the crater diameter and $\pi_d = d(\rho/m)^{1/3}$ for the crater depth, where ρ is the target material density, m the impactor mass, D the transient crater diameter and d the transient crater depth. Another important parameter, often called the gravity-scaled size, is defined as $\pi_2 = 1.61(gL)/U^2$ where g is the gravitational acceleration, L the impactor diameter and U the impact speed. Previous investigations on liquid impacts most commonly used the Froude number (e.g., Pumphrey & Elmore, 1990; Bisighini et al., 2010; Ray et al., 2015; Landeau et al., 2021; Lherm et al., 2022). With this formalism, the Froude number scales as $1/\pi_2$. We therefore use the Froude number, instead of π_2, in this study.

Impact outcomes have been measured in numerical simulations (e.g., Güldemeister et al., 2015; Hyodo & Genda, 2020) and laboratory experiments (e.g., Gault & Sonett, 1982; Schmidt & Housen, 1987). Crater formation upon impact is difficult to reproduce in the laboratory, especially because the velocity and size of impactors are limited in experiments. For example, the faster the impactor velocity, the smaller the projectile since it is technically very complicated to launch more than mm-sized competent compact projectiles at supersonic velocities. Indeed, to reach a given velocity, launching a larger projectile requires more energy, hence larger devices and it becomes technically increasingly

144 hard as the projectile size increases. Impact velocities are typically limited to a maxi-

145 mum of ∼6 km/s, while impacts in the solar system reach up to tens of km/s (e.g., Wether-

146 ill, 1996; Raymond et al., 2009). In solid impact experiments, the Froude number is or-

147 ders of magnitude larger than expected for planetary-scale impacts. In addition, in solids,

148 subsonic velocities are very hard to accomplish because of the material strength. In con-

149 trast, impact experiments of a solid projectile into a liquid can explore both subsonic and

150 supersonic regimes (Engel, 1967; Gault & Sonett, 1982; Schmidt & Housen, 1987; Lan-

151 deau et al., 2021). For impacts into liquid targets, as for impacts into solid targets, the

152 larger the impact launch speed, the smaller the mass and size of the projectile, hence the

153 larger the Froude number. This usually implies to have experiments performed in con-

154 ditions where the Froude number is way larger than the range expected for large craters

155 (typically $1 < Fr < 500$). High-velocity solid-into-liquid impact experiments have pro-

156 vided insightful results on the physical processes of crater formation in a liquid mate-

157 rial (e.g., Gault & Sonett, 1982; Schmidt & Housen, 1987). In particular, Gault and Sonett

158 (1982) have performed hypervelocity impacts of spherical projectiles into water. The pro-

159 jectiles are millimeter-sized pyrex grains and they are launched at velocities ranging from

160 1.25 to 6km/s with a vertical light-gas gun. The cratering processes have been captured

161 by a high-velocity camera, enabling the tracking of the crater depth as a function of time

162 during the crater opening. In these experiments, the Mach number, $M = U/U_s$, where

163 U_s is the sound speed in the target, ranges between 0.85 and 4.08 while the Froude num-

164 ber ranges from 10^8 to 4×10^9. Most of these experiments are comprised between $M =$

165 1 and $M = 2$ and only two experiments are conducted at $M > 2$. Peak shock pressures

166 produced in the projectile and water target are in the range of 250 to 300 GPa. Results

167 from these impact experiments have been compared to water drop experiments (see fig-

168 ure 9. in K. Holsapple & Schmidt, 1982). They show that the best-fit scaling for the crater

169 volume in hypervelocity impacts perfectly fits the water drop experiments once extrap-

170 olated over more than 6 orders of magnitude in the Froude number. This remarkable ex-

171 trapolation is however not fully understood. In particular, the transition regime from

172 subsonic to supersonic crater formation has not been explored, and our current knowl-

173 edge of energy and momentum transfer upon impacts does not explain such an extrap-

174 olation.

Table 1. Typical values of the Mach and Froude numbers for planetary impacts, the experiments and simulations of this study and the impact experiments onto water from Gault and Sonett (1982).

Dimensionless Number	Typical values for large planet-building impacts	Experiments (this study)	Experiments in Gault and Sonett (1982)	iSALE simulations (this study)
$\mathrm{Fr} = U^2/(gR)$	1 - 500	6 & 93	$\sim 10^6$ - 10^9	1 - 10^4
$\mathrm{M} = U/U_s$	1 - 10	9×10^{-4} & 3.6×10^{-3}	1 - 4	10^{-3} - 8

1.3 Objective of the study and summary

To investigate the impact-cratering process in liquid-liquid impacts at subsonic to supersonic velocities, we combine laboratory experiments (section 2.1) and impact numerical simulations (section 2.2). Most of the previous studies on impact cratering search for scaling laws for the crater diameter because this property is straightforward to compare with crater observations at the surface of planets. However, the crater diameter strongly depends on an arbitrary criterion that defines the crater edge. Thus, in this study, we choose to analyse the crater depth, instead of the diameter, because this quantity is more objectively defined as the lower edge of the crater and it can be measured in both experiments and simulations with a higher accuracy. Yet, crater diameter estimates from our simulations are discussed in Appendix B.

We first compare laboratory impact experiments at low velocities (M < 1) with numerical simulations in similar impact conditions (section 3). Our comparison validates the accuracy of the shock physics code iSALE for subsonic water-into-water impacts. iSALE is further used to test the influence of the Mach number on the maximum crater depth with a particular attention on the transition between the sub- and supersonic collisions (section 5). We finally discuss the transfer of energy upon planetary impacts (section 6) and its implications for the understanding of the cratering process (section 7).

2 Methods

In this section, we describe the methods for both water impact experiments and the numerical simulations used in our study. Table 1 gives the values of the Mach and Froude numbers explored in this study along with their typical values in planetary im-

pacts. These values are compared against those previously explored by Gault and Sonett (1982).

2.1 Water-impact experiments

Two experiments were chosen for this study. They are analogues for large impacts into a magma ocean. The experimental setup has been developed such that the dynamical regime in experiments is as close as possible to that of planetary impacts: the Froude number is within the range expected for large planet-building impacts (table 1) and inertia is large compared to viscous forces and surface tension, as detailed in Landeau et al. (2021). Previous experiments investigate the impact of millimetric drops onto a deep pool (e.g. Engel, 1967; Pumphrey & Elmore, 1990; Bisighini et al., 2010; Ray et al., 2015; Santini et al., 2017; Lherm et al., 2022). In contrast, we use much larger impactors with a radius $R \simeq 3$ cm. Because this size is large compared to the capillary length, surface tension is negligible and does not affect the cratering dynamics in our experiments. This result has been tested and quantified in Landeau et al. (2021) (see their section 4.2). Two different Froude numbers are used: Fr = 6 and Fr = 93. They correspond to the two extreme values that can be reached in this experimental setup and hence cover the entire experimental range. However, both experiments are subsonic with a Mach number M $< 3 \times 10^{-3}$.

The experimental setup is the same as the one presented in Landeau et al. (2021). The target is a pool of fresh water contained in an acrylic tank with a width of 75 cm. The water depth of the tank is 50 cm. The impactor is also made of fresh water. An impacting water volume of radius $R \simeq 3$ cm is initially held in a latex balloon at a controlled height above the target surface. The balloon latex membrane is broken by a needle at a height of less than 30 cm above the target surface. This release process ensures that the impacting water volume maintains a nearly spherical shape upon impact. The balloon little affects the crater formation process because it is tied to a string that prevents it from falling into the target. In some experiments, small pieces of balloon fall in the target but we do not observe any significant effect on the crater depth, as shown in Landeau et al. (2021). The two different Froude numbers are achieved by varying the release height that controls the impact speed. The velocity is 1.35 ± 0.1 m/s for the experiment with Fr = 6 and 5.3 ± 0.3 m/s for the experiment with Fr = 93. This change in impact velocity also affects the Mach number, but it remains much smaller than unity:

229   M= 9×10^{-4} for Fr = 6 and M = 3.6×10^{-3} for Fr = 93. Since water impacts onto wa-

230   ter in our experiments, the density difference between the target and the impactor is not

231   explored in this study. There is no difference in viscosity either. The gravity is that at

232   Earth surface: g = 9.81 g.m.s^{-2}. The detailed parameters for the two experiments are

233   given in the appendix A. The impact parameters and the maximum crater depth in these

234   two experiments, E1 & E2, are summarized in table 2.

2.2 Numerical modelling with iSALE

236   iSALE is a grid-based shock physics code that is well suited for planetary impacts

237   modelling (Amsden et al., 1980; Collins et al., 2002; Wünnemann et al., 2005). iSALE

238   has already been widely benchmarked and validated against observations in the hyper-

239   velocity regimes (e.g., Güldemeister et al., 2013; Kowitz et al., 2013). Its applicability

240   to subsonic impact velocities has, however, not yet been investigated. We employ iSALE

241   to model the impact of a liquid impactor into a liquid target and use a setup that cor-

242   responds to the conditons in the experiments presented in subsection 2.1. Due to the sym-

243   metry of vertical impacts we use iSALE-2D with a cylindrical axisymmetric grid. In a

244   first step we carried out a suite of simulations at subsonic conditions to validate our mod-

245   els by benchmarking them against the experiments presented in section 2.1. In a second

246   step we conducted a systematic study of numerical impact experiments at supersonic im-

247   pact velocities. Several materials are studied for comparison (water, aluminium, iron and

248   basalt) however the simulations are purely hydrodynamical as we do not consider any

249   material strength. We only consider homogeneous projectiles. The impact angle is kept

250   constant in this study; all our experiments and simulations are head-on impacts. For wa-

251   ter, aluminium, iron and basalt, the Tillotson (Tillotson, 1962) equation of state (EoS)

252   is used. We use the planar target approximation, which assumes that the target's free

253   surface is an infinite horizontal plan, hence excluding any geometrical effects of the tar-

254   get's curvature. We focus here on the formation and collapse of the impact crater. , which

255   is why we did not run the models until the very end of the crater formation process, when

256   the target is fully equilibrated. Instead, we stop most of our simulations after the ex-

257   cavation stage, at some time during the modification stage, to save computation time.

258   The spatial resolution varies from 20 to 25 CPPR (Cells Per Projectile Radius).   For

259   the sake of simplicity, the thermal profile in the target is considered uniform before the

260   impact. All simulations analyzed in this study are listed in table 2 and table 3.

Table 2. Data used in this study, including the experiments E1 & E2 and the entire set of iSALE numerical simulations The first column, ID, refers to the name that are given to the different experiments/simulations. The type indicates whether it corresponds to a water impact experiment or to an impact simulation with iSALE. The material corresponds to the Tillotson equation of state that has been used for both the target and impactor in the case of iSALE simulations. In the experiments, the target and impactor material is water. For each experiment and simulation, the values of the impact velocity, U, the impactor radius, R, the Mach number, M, and the Froude number, Fr, are given. The gravity is g = 9.81 m.s^{-2} in all simulations and experiments. The respective sound velocities for water, basalt, aluminium and iron are: 1481 m/s, 4472 m/s, 5277 m/s and 4051 m/s. Resolution for water simulations is 20 CPPR. For all other simulations, resolution is 25 CPPR.

| General information		Impact conditions					Crater
ID	Type	material	U (m/s)	R (m)	M	Fr	Z_c (m)
E1	experiment	water	1.35E+00	3.05E-02	9.00E-04	6.00E+00	5.03E-02
E2	experiment	water	5.30E+00	3.08E-02	3.60E-03	9.30E+01	9.97E-02
E1_1	simulation	water	1.05E+01	1.83E+00	7.00E-03	6.00E+00	3.26E+00
E1_2	simulation	water	1.14E+01	2.21E+00	7.7E-03	6.00E+00	3.86E-03
E1_3	simulation	water	1.29E+02	2.85E+00	8.75E-03	6.00E+00	4.99E-03
E1_4	simulation	water	1.77E+01	5.37E+00	1.20E-02	6.00E+00	9.33E-03
E1_5	simulation	water	2.07E+01	7.30E+00	1.40E-02	6.00E+00	1.26E-02
E1_6	simulation	water	1.48E+02	3.73E+02	1.00E-01	6.00E+00	6.52E-01
E1_7	simulation	water	1.48E+03	3.73E+04	1.00E+00	6.00E+00	6.20E+04
E2_1	simulation	water	4.14E+02	1.88E+00	2.80E-02	9.30E+01	6.25E-03
E2_2	simulation	water	6.37E+01	4.40E+00	4.30E-02	9.30E+01	1.47E-02
E2_3	simulation	water	4.88E+01	2.62E+00	3.30E-02	9.30E+01	8.70E+00
E2_4	simulation	water	5.55E+01	3.38E+00	3.75E-02	9.30E+01	1.13E+01
E2_5	simulation	water	7.85E+01	6.75E+00	5.30E-02	9.30E+01	2.25E+01
E2_6	simulation	water	8.89E+01	8.60E+00	6.00E-02	9.30E+01	2.87E+01
E2_7	simulation	water	1.48E+02	2.40E+01	1.00E-01	9.30E+01	7.99E-02
E2_8	simulation	water	3.70E+03	1.50E+04	2.50E+00	9.30E+01	4.62E+04
E2_9	simulation	water	7.41E+03	6.01E+04	5.00E+00	9.30E+01	1.55E+05
E2_10	simulation	water	4.44E+02	2.16E+02	3.00E-01	9.30E+01	7.29E+02
E2_11	simulation	water	7.41E+02	6.01E+02	5.00E-01	9.30E+01	2.02E+03
E2_12	simulation	water	1.04E+03	1.18E+03	7.00E-01	9.30E+01	3.98E+03
sim170	simulation	water	3.11E+03	9.76E+03	2.10E+00	1.01E+02	3.12E+04
sim18	simulation	water	1.93E+03	4.66E+03	2.10E+00	8.10E+01	1.47E+04
simv2_213	simulation	water	4.59E+03	3.26E+04	3.10E+00	6.60E+01	8.90E+04
sim3	simulation	water	1.63E+03	8.70E+03	1.10E+00	3.10E+01	2.18E+04
simv22	simulation	water	7.41E+03	4.66E+03	5.00E+00	1.20E+03	2.29E+04
simv27	simulation	water	8.89E+03	4.70E+03	6.00E+00	1.70E+03	2.40E+04
v3Fr5	simulation	water	1.00E+04	1.02E+03	6.75E+00	1.00E+04	7.39E+03
v1Fr2	simulation	water	1.00E+03	1.02E+03	6.75E-01	1.00E+02	3.44E+03
Al_M10-3	simulation	aluminium	5.28E+00	5.00E-01	1.00E-03	5.68E+00	8.62E-01
Al_M10-2	simulation	aluminium	5.28E+01	1.00E+01	1.00E-02	2.84E+01	2.53E+01
Al_M10-1	simulation	aluminium	5.28E+02	1.00E+03	1.00E-01	2.84E+01	2.53E+03
Al_M0-5	simulation	aluminium	2.64E+03	1.00E+04	5.00E-01	7.10E+01	3.14E+04
Al_M1	simulation	aluminium	5.28E+03	1.00E+04	1.00E+00	2.84E+02	4.21E+04
Al_M2	simulation	aluminium	1.06E+04	1.00E+04	2.00E+00	1.14E+03	5.39E+04
Al_M3	simulation	aluminium	1.58E+04	5.00E+04	3.00E+00	5.11E+02	2.17E+05
Al_M4	simulation	aluminium	2.11E+04	5.00E+04	4.00E+00	9.09E+02	2.36E+05

Table 3. Data used in this study, including the experiments E1 & E2 and the entire set of iSALE numerical simulations. The first column, ID, refers to the name that are given to the different experiments/simulations. The type indicates whether it corresponds to a water impact experiment or to an impact simulation with iSALE. The material corresponds to the Tillotson equation of state that has been used for both the target and impactor in the case of iSALE simulations. In the experiments, the target and impactor material is water. For each experiment and simulation, the values of the impact velocity, U, the impactor radius, R, the Mach number, M, and the Froude number, Fr, are given. The gravity is g = 9.81 m.s^{-2} in all simulations and experiments. The respective sound velocities for water, basalt, aluminium and iron are: 1481 m/s, 4472 m/s, 5277 m/s and 4051 m/s. Resolution for water simulations is 20 CPPR. For all other simulations, resolution is 25 CPPR.

General information		Impact conditions					Crater
ID	Type	material	U (m/s)	R (m)	M	Fr	Z_c (m)
Al_M5	simulation	aluminium	2.64E+04	5.00E+04	5.00E+00	1.42E+03	2.22E+05
Al_M6	simulation	aluminium	3.17E+04	5.00E+04	6.00E+00	2.04E+03	2.09E+05
Al_M7	simulation	aluminium	3.69E+04	5.00E+04	7.00E+00	2.78E+03	2.71E+05
Al_M8	simulation	aluminium	4.22E+04	5.00E+04	8.00E+00	3.63E+03	2.64E+05
Al_M9	simulation	aluminium	4.75E+04	5.00E+04	9.00E+00	4.60E+03	2.38E+05
Ba_M10-3	simulation	basalt	4.47E+00	5.00E-01	1.00E-03	4.08E+00	7.99E-01
Ba_M10-2	simulation	basalt	4.47E+01	1.00E+01	1.00E-02	2.04E+01	2.33E+01
Ba_M10-1	simulation	basalt	4.47E+02	1.00E+03	1.00E-01	2.04E+01	2.33E+03
Ba_M0-5	simulation	basalt	2.24E+03	1.00E+04	5.00E-01	5.10E+01	2.89E+04
Ba_M1	simulation	basalt	4.47E+03	1.00E+04	1.00E+00	2.04E+02	3.92E+04
Ba_M2	simulation	basalt	8.94E+03	1.00E+04	2.00E+00	8.15E+02	5.03E+04
Ba_M3	simulation	basalt	1.34E+04	5.00E+04	3.00E+00	3.67E+02	2.00E+05
Ba_M4	simulation	basalt	1.79E+04	5.00E+04	4.00E+00	6.52E+02	2.16E+05
Ba_M5	simulation	basalt	2.24E+04	5.00E+04	5.00E+00	1.02E+03	2.27E+05
Ba_M6	simulation	basalt	2.68E+04	5.00E+04	6.00E+00	1.47E+03	2.35E+05
Ba_M7	simulation	basalt	3.13E+04	5.00E+04	7.00E+00	2.00E+03	2.28E+05
Ba_M8	simulation	basalt	3.58E+04	5.00E+04	8.00E+00	2.61E+03	2.24E+05
Ba_M9	simulation	basalt	4.02E+04	5.00E+04	9.00E+00	3.30E+03	2.35E+05
Fe_M10-1	simulation	iron	4.05E+02	1.00E+03	1.00E-01	1.67E+01	2.22E+03
Fe_M0-5	simulation	iron	2.03E+03	1.00E+04	5.00E-01	4.18E+01	2.77E+04
Fe_M1	simulation	iron	4.05E+03	1.00E+04	1.00E+00	1.67E+02	3.75E+04
Fe_M2	simulation	iron	8.10E+03	1.00E+04	2.00E+00	6.69E+02	4.81E+04
Fe_M3	simulation	iron	1.22E+04	5.00E+04	3.00E+00	3.01E+02	1.90E+05
Fe_M4	simulation	iron	1.62E+04	5.00E+04	4.00E+00	5.35E+02	2.06E+05
Fe_M5	simulation	iron	2.03E+04	5.00E+04	5.00E+00	8.36E+02	2.15E+05
Fe_M6	simulation	iron	2.43E+04	5.00E+04	6.00E+00	1.20E+03	1.98E+05

3 Subsonic impacts: validation of numerical simulations against experiments

3.1 Qualitative description

The two experiments that are described in section 2.1 are qualitatively compared with iSALE simulations at subsonic impact velocities (M < 1) and at the same Froude numbers. Figure 1 shows the dynamics in these experiments and simulations. The up-
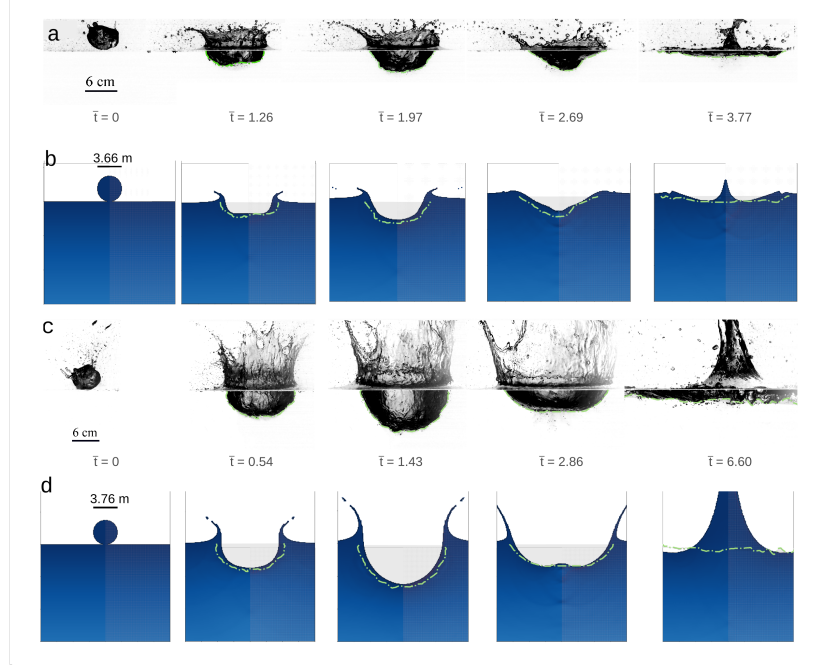
Figure 1. Snapshots of laboratory experiments (a and c) and iSALE simulations (b and d) for subsonic impacts (M << 1) at Fr = 6 (a and b) and Fr = 93 (c and d). The Mach number is M = 9×10^{-4} in a, M = 7×10^{-3} in b, M = 3.6×10^{-3} in c and M = 2.8×10^{-2} in d. b shows snapshots from the simulation E1_1 and d snapshots from E2_1 (see table 2). The different shades of blue refer to the pressure field. The light green curves correspond to the crater profile from the experiments superposed onto the simulation snapshots, once rescaled to the impactor radius. The dimensionless time, $\bar{t} = \frac{t}{\sqrt{R/g}}$, is displayed for each snapshot.

per panel corresponds to the impact with Fr = 6 in both experiments and simulations while the lower panel shows the case Fr = 93. Although the numerical simulations and the laboratory experiments have the same Froude and Mach number the dimensions deviate. To make the snapshots comparable, we normalise the time by the $\sqrt{R/g}$. In all cases, the first snapshot shows the pre-impact conditions. The second snapshot shows the cratering state after a few milliseconds, as the impactor penetrates through the tar-

get and opens a crater. This stage lies in between the contact and compression stage and the crater excavation stage of impact cratering (Melosh, 1989).   . However, in the case of a subsonic impact, there is no compression stage, which is defined as the duration needed for the shock wave and subsequent rarefaction wave to travel through the entire projectile. Thus, no material compression occurs in the impacts shown in figure 1, and the crater starts opening because the kinetic energy of the impactor is converted into flow motions in the target. The third snapshot illustrates the time when the crater has reached its maximum depth . This corresponds approximately to the end of the crater excavation stage (even if the crater may still grow laterally) and the beginning of the crater modification stage during which the crater collapses. Finally, on the last snapshot, the formation of a jet is observed in both experiments and numerical modelling. In summary, the snapshots in figure 1 demonstrate that iSALE simulations qualitatively reproduce the laboratory experiments. The crater shape, together with the crater depth are very similar in simulations and experiments (see green dotted curves on figure 1).

3.2 Crater depth as a function of time

To quantify the agreement between experiments and simulations, figure 2 shows the evolution of the crater depth normalised by the impactor radius as a function of the dimensionless time normalised by $\sqrt{R/g}$. The experimental results are shown in red (dotted line for Fr = 93 and plain line for Fr = 6). Curves with different shades of gray show simulation runs for different Mach numbers, ranging from M = 2.3×10^{-2} in dark gray to M = 0.7 in light gray. All simulations shown in figure 2 are at subsonic conditions. They are indistinguishable from one another, and from the experimental curves. Both the trend and amplitudes are similar, which confirms that iSALE is applicable to simulate subsonic liquid impacts. It also shows that, in the subsonic case, the effect of the Mach number is negligible and only the Froude number controls the cratering process.

3.3 Maximum crater depth: effects of the Froude number

As shown in previous studies (e.g., K. Holsapple & Schmidt, 1982; K. A. Holsapple, 1993; O'Keefe & Ahrens, 1993; Landeau et al., 2021), the normalised maximum crater depth Z_c/R increases with the Froude number. This is illustrated in figure 3, which shows all the iSALE runs performed with Fr = 6 and Fr = 93 for water impacts. The different Mach numbers are indicated by using varying shades of gray. In this section, we fo-
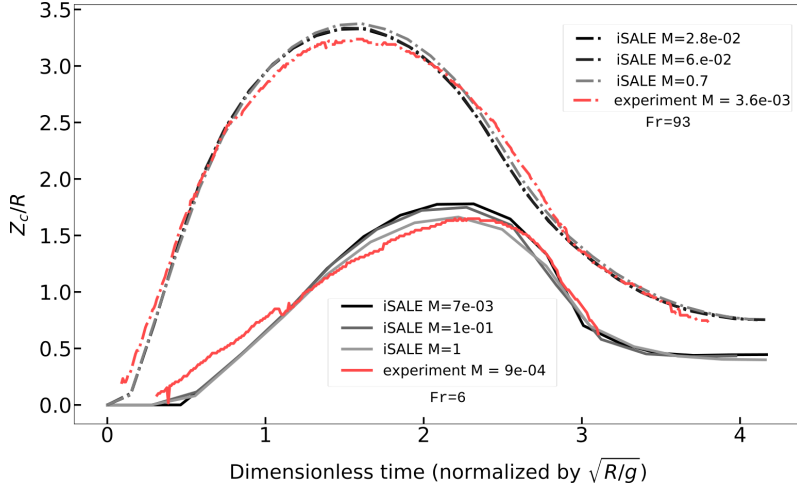
Figure 2. Comparison between crater growth in laboratory experiments and numerical simulations. The crater depth Z_c is normalised by the impactor radius R and time is normalised by $\sqrt{R/g}$, so that both parameters are dimensionless (see section 2.1). The two red curves correspond to two experiments with Froude number Fr = 6 (plain curve) and Fr = 93 (dotted curve). Both are subsonic (M < 1). Gray curves are results for subsonic impact simulations with the same Froude numbers as the experiments (plain curves for Fr = 6 and dotted curves for Fr = 93). The different shades of gray correspond to different Mach numbers.

cus on subsonic impacts, and hence only on the darker gray points in figure 3. When the Mach number is below unity, the data from iSALE simulations agree well with the scaling for subsonic impacts into water (Landeau et al., 2021). This scaling is a power-law of the form $Z_c/R = a\,Fr^{\mu}$, where a = 1.1 ± 0.05 and μ = 0.24 ± 0.01 are imperically determined fitting parameters. This scaling however neglects the effect of the Mach number. This may explain why the results of our simulations with M > 1 do not fall on the red dashed lines in figure 3. To better understand these findings, we need to investigate the transition from the subsonic to the supersonic regime.

4 Supersonic impacts: effect of the Mach number

In the supersonic case, a shock wave is generated upon impact. This is visible in figure 4 where different snapshots of a supersonic case (Ba_M5, see table 3) are shown. The pressure field in the target is shown in blue. The shock wave generation and propagation is visible as the shock corresponds to a jump in pressure. Behind the shock front, the rarefaction wave is also visible as a decrease in pressure. The rarefaction propagates faster than the shock wave and eventually catches up with the shock front. The crater depth keeps growing until a dimensionless time $\bar{t} = t/\sqrt{R/g}$ of about 1.4, after which
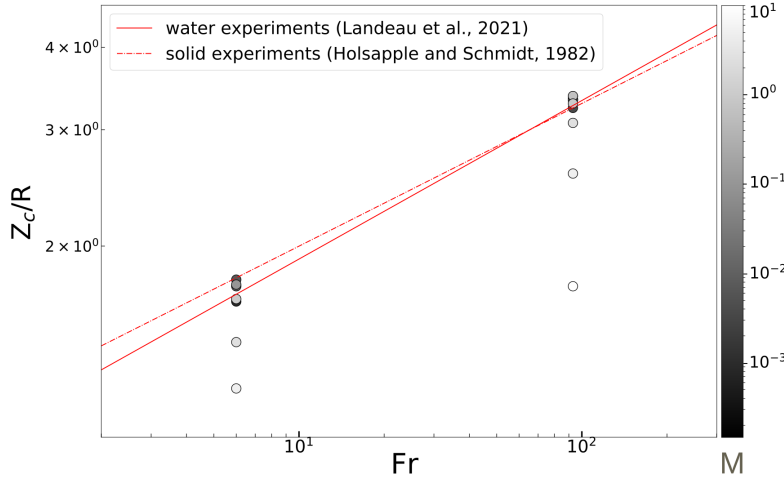
Figure 3. Maximum crater depth, Z_c, normalised by the impactor radius R, as a function of the Froude number for different numerical simulations of water into water impacts performed with iSALE and with Fr = 6 and Fr = 93. Two scaling laws from the litterature are shown by red lines: $Z_c/R = 1.216 \times \mathrm{Fr}^{0.216}$ for hypervelocity impacts of solid projectiles into water (K. Holsapple & Schmidt, 1982), and $Z_c/R = 1.1 \times \mathrm{Fr}^{0.24}$ for subsonic impacts of water volumes into water (Landeau et al., 2021). The shade of gray inside each symbol indicates the value of the Mach number.

320   it starts collapsing, while the horizontal extent of the crater close to the surface still in-

321   creases. Subsequently, at $\bar{t}$=2.44 the crater floor collapses and a central peak starts to

322   rise ($\bar{t}$=3.95). Regarding the crater depth, figure 5 shows that the subsonic and the hy-

323   personic cases are undistinguishable at early times ($\bar{t} < 0.5$ for Fr = 93 and $\bar{t} < 1$ for Fr

324   = 6). However, at later times, the crater depth grows less rapidly at higher Mach num-

325   bers (discussed in section 5). Light gray symbols in figure 3 and gray curves in figure 5

326   show that the maximum crater depth decreases with increasing Mach number when M>1.

327   . This suggests that the effect of the Froude number and the Mach number on the cra-

328   tering process must be considered independently from one another, and the scaling laws

329   for the maximum crater depth should be adjusted accordingly.

5 Crater depth scaling: transition from subsonic to supersonic impacts

331   In subsonic impacts, the normalised maximum crater depth, Z_c/R, has been shown

332   to scale as the Froude number to the power 1/4 (e.g., Melosh, 1989; Pumphrey & Elmore,

333   1990; Miranda & Dowling, 2019). This scaling arises from an energy balance reasoning.

334   Assuming that the impactor kinetic energy from the projectile is fully converted into

335   gravitational potential energy in a hemispherical crater , one obtains that: $m_i U^2 \propto \rho_t g Z_c^4$,
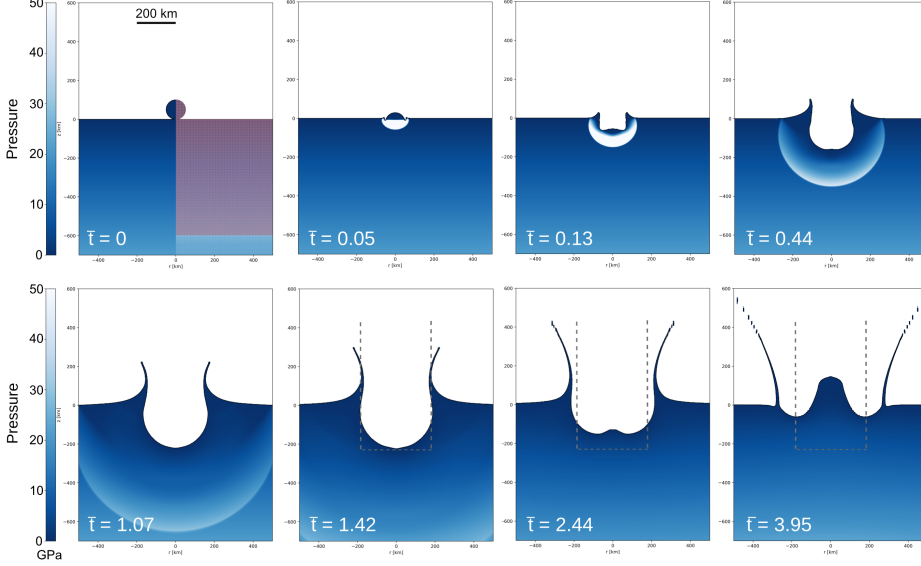
Figure 4. Snapshots of the crater evolution in the iSALE simulation *Ba_M5* (cf table 3). The blue colorbar corresponds to the pressure in the material. The dimensionless time $\bar{t} = t/\sqrt{R/g}$ is indicated in each snapshot. The first snaphsot highlights the computational domain grid on the right hand side. The maximum crater depth, and the associated crater diameter, are shown by gray dashed lines at a dimensionless time, $\bar{t}$, of 1.42 by grey dashed lines. These lines are reported on the later snapshots for comparison.

where m_i is the impactor mass, ρ_t the target density and g the target gravity. This re-lationship can be rewritten as $Z_c^4 \propto \frac{\rho_i R^3 U^2}{\rho_t g}$, with ρ_i the impactor density . As, in this study, the densities of the impactor and the target are the same, we obtain

$$Z_c/R \propto Fr^{1/4}. \tag{1}$$

It is well accepted that this pure energy scaling holds for subsonic impacts but breaks under supersonic conditions (Melosh, 1989; K. A. Holsapple, 1993). In order to analyse the transition regime from subsonic to supersonic impacts in more details, we therefore divide the normalised maximum crater depth Z_c/R by $Fr^{0.25}$. This normalisation is par-ticularly useful when comparing impacts with various Froude and Mach numbers. With this normalization we remove the effect of the Froude number on the maximum crater depth and emphasize the sole effect of the Mach number. This is illustrated in figure 5 where the time-evolution of the crater depth normalised by $Fr^{1/4}$ is shown for our two experiments and for iSALE simulations at different Mach numbers. In this figure, the different Froude number cases are hardly distinguishable from one another when M is below unity. This demonstrates that the subsonic scaling (1) is well satisfied by our ex-
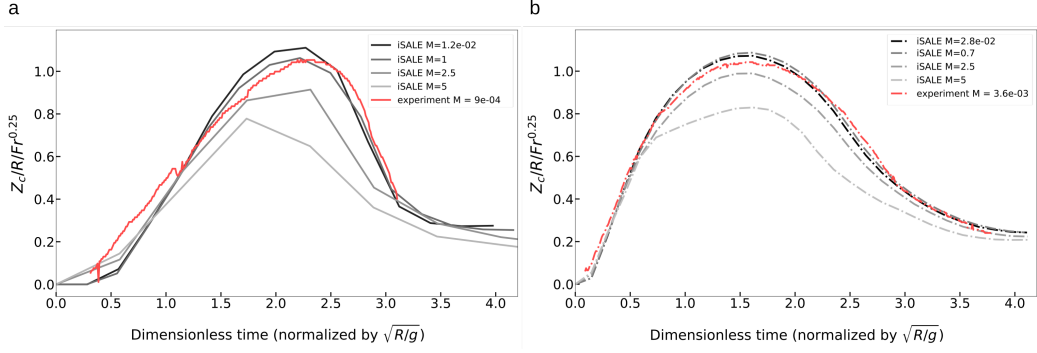
Figure 5. Time-evolution of the normalised crater depth in laboratory experiments and numerical simulations for Fr = 6 (a) and Fr = 93 (b). The red curves show the experiments while the gray curves correspond to different iSALE impact simulations. The figure is similar to figure 2, but the dimensionless crater depth Z_c/R is further normalised by the Froude number to the power 1/4 to ensure that the deviation from the subsonic cases when increasing the Mach number is not due to a change in the radius of the projectile (that has to be increased to increase M while conserving Fr). Note that the curves corresponding to the two highest M for Fr = 6 (i.e. panel a, M = 2.5 and M = 5) are less resolved (as suggested by the "broken" appearance of the curves). In that particular case, they are simply used for the comparison to subsonic cases at Fr = 6 but excluded from the data set used in the final fit (2).
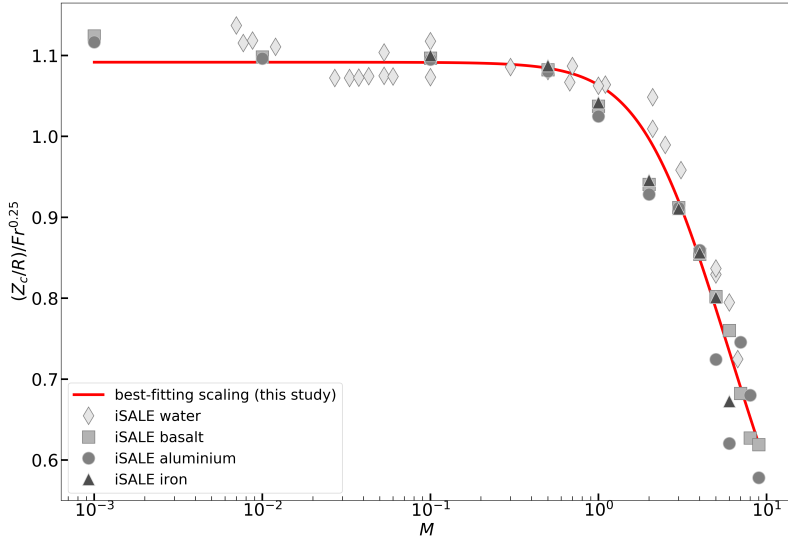
Figure 6. Evolution of the normalised maximum crater depth as a function of the Mach number M. The maximum crater depth Z_c is normalised by the pure energy scaling R $Fr^{1/4}$, which is expected for subsonic impacts (e.g., K. Holsapple & Schmidt, 1982; K. A. Holsapple, 1993). We fit our data by a function of the form $(Z_c/R)/Fr^{0.25} = a(1+bM^2)^{-c}$ (Miranda & Dowling, 2019). Using the method of least squares, we obtain the following best-fit coefficients: a = 1.092±0.006, b = 0.11±0.03 and c = 0.25±0.03. Different materials are tested in order to cross-check the behavior, using different equations of state.

periments and simulations with M < 1. However, iSALE results for hypervelocity im-
pacts (at M = 2.5 and M = 5) deviate from the subsonic cases: the maximum crater depth
decreases with increasing Mach number. Light gray symbols in figure 3 also illustrates
this trend. Figure 5 additionally confirms that this trend results from the effect of the
Mach number and not from a change in impactor size in the simulations.

To describe this effect of the Mach number, independently of the Froude number,
we follow the approach proposed by Miranda and Dowling (2019) for impacts into gran-
ular material. They proposed a relationship between the crater diameter, the Froude num-
ber and the Mach number based on energy partitioning and dimensional analysis. They
analysed crater dimensions from numerous existing experiments in granular materials
and, in agreement with previous studies (e.g., Schmidt, 1980; K. A. Holsapple, 1993),
found that the crater diameter in supersonic impacts increases more slowly with the Froude
number than in the subsonic case. This suggests an additional sink of energy in super-
sonic impacts, which decreases the energy available for the excavation of the crater. To
describe this relative decrease in crater diameter, they assume that the crater diameter
scales as $Fr^{1/4} f(M)$, where f(M) is only a function of the Mach number. To further spec-
ify $f(M)$, they make an analogy with the loss of total pressure across a shock wave in
a perfect gas. Total pressure is an analogue for the impactor kinetic energy per unit vol-
ume. Based on this analogy, they suggest that the fraction of the impactor energy that
is partitioned into the excavation of the crater scales as $(1 + bM^2)^{-4c}$, where a and c
are positive coefficients to be determined emperically. This implies that the fraction of
energy that goes into the crater excavation decreases with increasing Mach number. The
scaling also implies that the dimensionless crater diameter scales as $Fr^{1/4}(1+aM^2)^{-c}$
(equation (11) in Miranda and Dowling (2019)).

The rationale by Miranda and Dowling (2019) also holds for impacts into a liquid.
We therefore assume that the crater depth follows the scaling

$$(Z_c/R)/Fr^{1/4} = a(1 + bM^2)^{-c}, \qquad (2)$$

where a, b and c are best-fit parameters. Applying the method of least squares to our
numerical data, we find that a = 1.092 ± 0.006, b = 0.11 ± 0.03 and c = 0.25 ± 0.03.
We obtain a good fit of our data with a coefficient of determination, R^2, of 0.959. We
computed the coefficients a, b and c for each material used in our simulations (water,

basalt, aluminium and iron) but we did not find any significant difference in their values for different materials.

Figure 6 shows the maximum crater depth, normalised by $R\,Fr^{1/4}$ from iSALE numerical simulations performed for different materials (water, basalt, aluminium and iron) as a function of the Mach number. All data points collapse on the same trend, which is well described by equation (1). For M < 1, figure 6 and scaling (2) shows that the pure energy scaling (1) is well satisfied by our data. However, for M > 1, the normalised crater depth Z_c/R decreases with increasing Mach number. This suggests that some fraction of the kinetic energy of the impactor goes into the generation and propagation of a shock wave. The energy that is initially consumed by the shock wave transitions into heat dissipation, material compression/destruction and the formation of a high velocity hot ejecta plume. In particular, the mass and kinatic energy that are transferred to the ejecta (some even gravitationally escaping the entire system) are lost from the system, and hence likely contribute to the difference in crater depth between subsonic and supersonic cases. When the supersonic regime starts at M > 1, scaling (2) together with the positive value of c, indicate that the fraction of energy that is partitioned into the shock wave increases with increasing Mach number. To confirm this hypothesis in the following subsection, we analyse in detail the energy partitioning in our simulations comparing the regimes M < 1 and M > 1.

6 Analysis of the energy partitioning with time

The diminution of Z_c/R observed when M>1 (figure 6) could result from an increase in the compression of the impacting and target materials. In the hypervelocity regime, the crater excavation is controlled by nonisentropic shock compression of the material instead of an incompressible displacement of the material (i.e. target kinetic energy). This is further discussed in section 7.1.

To estimate the energy partitioning with time in iSALE simulations, we compute the kinetic energy in the impactor, the kinetic energy in the target, and the internal energy in the target (as detailed in appendix C). We assume that the difference between the initial impactor kinetic energy and these energies corresponds to the gravitational potential energy which is given by the crater size, the kinetic energy of the ejecta and the jet. The results are shown in figure 7 for two simulations of a basaltic projectile impacting onto a basaltic target layer. The left panel (fig. 7a.) shows the energy par-

413 titioning in a subsonic case while the right panel (fig. 7b.) shows a supersonic case at

414 M=5.
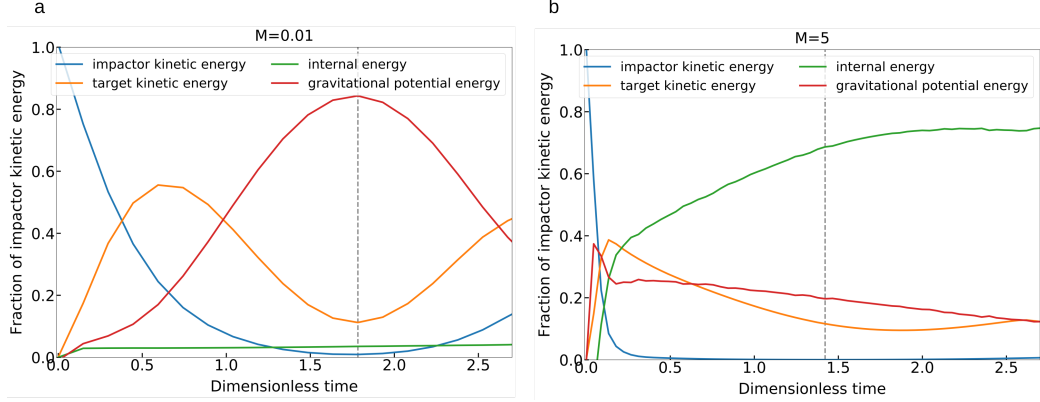
Figure 7. Energy partitioning upon impact (a) shows Ba_M10-2 (see table 3), a basalt-into-basalt collisions at low Mach number ($M = 10^{-2}$) and (b) shows Ba_M5 (see table 3), a supersonic case with $M = 5$. Colors show the different energy fractions relative to the initial impactor kinetic energy. The results are shown as a function of the dimensionless time $t/\sqrt{R/g}$. The gray dashed lines locate the time of maximum crater depth.

415 Under subsonic conditions (figure 7a), the impactor kinetic energy is smoothly trans-

416 ferred into the target as the target material is pushed aside and displaced upon projec-

417 tile. After some time, the displacement of the target stops and the crater reaches its max-

418 imum size around a dimensionless time of 1.78. This time corresponds to the maximum

419 in gravitational potential energy and a local minimum in target kinetic energy. The ki-

420 netic energy then increases again as target material starts to rise forming a central splash

421 or jet. At this stage, the velocity is orientated upward instead of downward. The con-

422 sumption of energy by the formation of the jet also explains the increase in the impactor

423 kinetic energy as both target and impactor materials are entrained into the jet. Only a

424 very low fraction of internal energy is produced when M < 1.

425 Figure 7b. reveals different dynamics in the supersonic case M = 5. The most strik-

426 ing difference is the high values of the internal energy (green curve). Additionally, the

427 impactor kinetic energy drops more rapidly and is quickly transferred into the target,

428 mostly as internal energy. After $\bar{t} \simeq 0.1$, both the fractions of gravitational potential en-

429 ergy and target kinetic energy decrease as they are also transferred into internal energy.

430 The target kinetic energy keeps decreasing, until $\bar{t} \simeq 1.7$, which corresponds to the point

431 in the time when the maximum crater depth is reached. This is due to the lateral growth

432 of the crater, which lasts longer than the vertical crater growth. The time evolution of

433 the internal energy, and especially the relative partitioning between compression and heat-

434 ing requires further investigation and will be the focus of a follow-up study.

7 Discussion and implications

7.1 Maximum crater depth for very large Mach number

437 Our new scaling (2) for the maximum crater depth has important implications for

438 impact cratering in the limit of large Mach numbers. When the Mach number is large

439 enough, the term bM^2 becomes larger than 1 in equation (2), and the crater depth sat-

440 isfies

$$\frac{Z_c}{R} \propto Fr^{1/4}M^{-2c}. \tag{3}$$

442 Our best-fit coefficient c = 0.25±0.03 suggests that

$$\frac{Z_c}{R} \propto Fr^{1/4}M^{-1/2}. \tag{4}$$

444 Replacing the Mach number and the Froude number by their respective expressions, one

445 gets

$$\frac{Z_c}{R} \propto \left(\frac{U^2}{gR}\right)^{1/4}\left(\frac{U}{U_s}\right)^{-1/2}, \tag{5}$$

447 with U_s the sound velocity in the pre-shocked material. This finally yields

$$\frac{Z_c}{R} \propto (gR)^{-1/4}U_s^{1/2}. \tag{6}$$

449 Relation (6) suggests that, when the Mach number approaches infinity, the crater ex-

450 cavation becomes independent of the impact velocity and is instead limited by the sound

451 velocity of the impacted material. To check whether this change in regime is visible in

452 our iSALE simulations, we introduce a "sound Froude" number that is defined as $Fr_s = U_s^2/gR$.

453 Equation 6 then becomes:

$$\frac{Z_c}{R} \propto Fr_s^{1/4}. \tag{7}$$

455 Relation (7) implies that, in the limit of large Mach numbers, the crater depth is con-

456 trolled by the ratio of the sound speed squared to the weight of the impactor. We test

457 this behavior in figure 8, which shows Z_c/R normalised by $Fr_s^{1/4}$ as a function of the

458 Mach number. As the Mach number increases, the increase in $Z_c/(RFr_s^{1/4})$ gets slower.

459 The data approaches a plateau for M > 5. The plateau in figure 8 agrees with scaling (7)

460 and confirms that the maximum crater depth is limited by the sound velocity for large

461 Mach numbers. This limitation in crater depth is likely related to the compression stage.
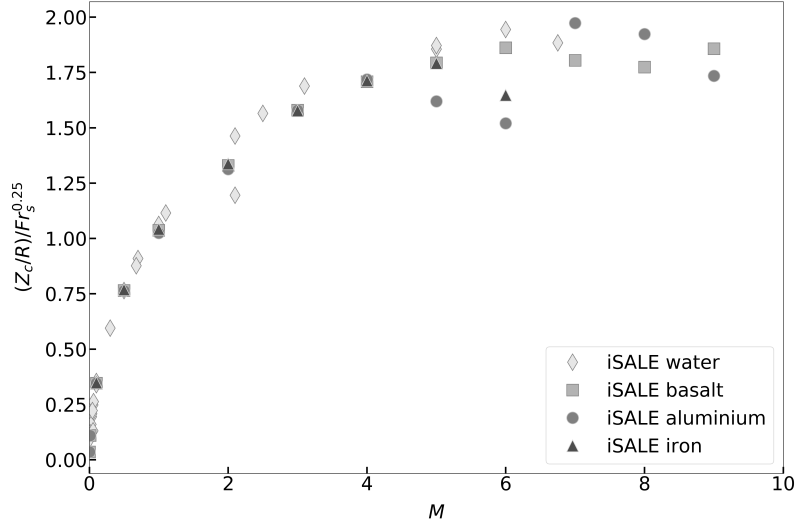
Figure 8. Maximum crater depth normalised by $\mathrm{RFr}_s^{0.25}$ as a function of the Mach number for the different iSALE simulations performed for different materials, with $\mathrm{Fr}_s = U_s^2/(gR)$ for all the simulations performed.

In a fluid, the sound velocity is $\sqrt{K/\rho}$, where K is the bulk modulus. The bulk modulus is a measure of the resistance of a given material against compression. Accordingly, the larger K, the higher the sound velocity and the resistance against compression. During an impact, if the impact velocity is much larger than the sound speed, it is rather intuitive that the crater excavation should be limited by the capacity of a material to resist compression. This behavior is consistent with the previous sections, which suggest that, at large Mach numbers, the crater opening is mostly controlled by the compression during the shock instead of the kinetic energy in the target. Above a certain impact velocity, further addition of kinetic energy does not generate more compression because the degree of compressibility of the material has been over-passed already. No matter how much more energy is brought to the system, it cannot be transferred in compression anymore, and is thus expected to be transferred into heat in the target. We therefore speculate that for very large impact-to-sound speed ratios, adding more kinetic energy to the system would result in more heating and more melting and/or vaporization, but not in a further increase of the crater depth.

7.2 Comparison to previous studies and to the π-group scaling

As mentioned in section 1.2, one of the most remarkable results from previous studies on impacts into a liquid target is the successful extrapolation, to subsonic impacts, over several orders of magnitude in Froude or π_2 number, of the hypervelocity scaling for the crater efficiency (K. Holsapple & Schmidt, 1982) . The hypervelocity data used in this scaling are reported in figure 9 (Gault & Sonett, 1982). Along with those data, we show our scaling law (2) for different Mach numbers in figure 9. Indeed, in the scaling equation (2), the Froude number, and hence π_2, is independent from the Mach number. The Mach number is between 1 and 4 in the impact experiments of Gault and Sonett (1982). Meanwhile, π_2 varies in the range $2\times10^{-9}-10^{-8}$ in the data set used by Gault and Sonett (1982) and in the range $10^{-4}-10^{-2}$ in the subsonic impacts to which K. Holsapple and Schmidt (1982) extrapolate into the hypervelocity regime. Figure 9 shows that, for M in the range 1-4, the crater depth deviates by only ∼20% from the pure energy scaling at M < 1. This deviation is small compared to the variation of more than one order of magnitude in crater depth due to the variation in π_2 between the hypervelocity data used by Gault and Sonett (1982) and the subsonic impacts. This explains why the extrapolation of the hypervelocity scaling to subsonic impacts gives reasonable estimates of the crater efficiency and the crater depth. However, figure 9 also demonstrates that, for more accurate predictions, the effect of the Mach number should be taken into account. In particular, in the regime $10^{-4} < \pi_2 < 1$, corresponding to large planetary impacts (figure 9.b), the data with M > 3 deviate significantly from the pure energy scaling or the π-group scaling of Schmidt and Housen (1987) (see dark gray circular points on figure 9) .

7.3 Different materials

As discussed previously, the nature of the material will influence the maximum crater depth through the sound speed. However, data from different materials collapse on the same master curve when plotted as a function of the impact-to-sound speed, i.e. the Mach number (figure 6). This suggests that differences in the equation of state of the different materials have a negligible effect on the crater depth.
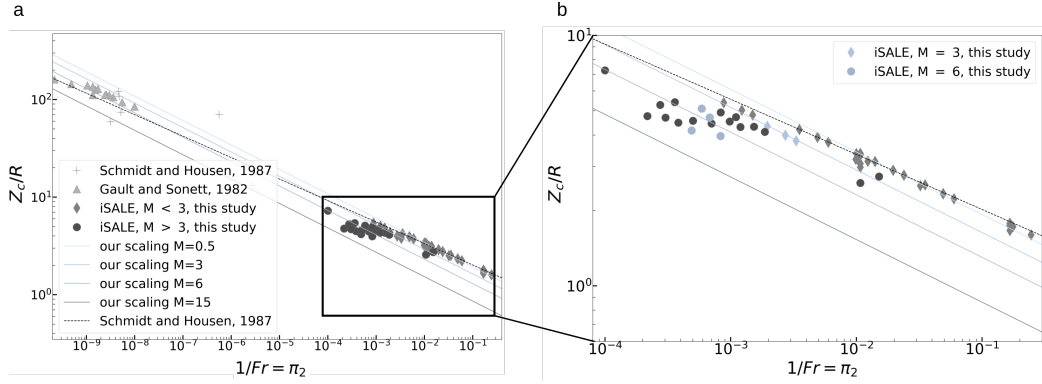
Figure 9. Normalised maximum crater depth, Z_c/R, as a function of $1/\mathrm{Fr} \propto \pi_2$. The data from previous studies (Schmidt & Housen, 1987; Gault & Sonett, 1982) are shown along with different light-blue-shaded lines corresponding to scaling (2) for different values of the Mach number. The dashed black line shows the scaling law $Z_c/R = 1.216 Fr^{0.22}$ given by Schmidt and Housen (1987) for supersonic impacts into a liquid. Panel (a) shows all data while the panel (b) zooms on $1/\mathrm{Fr}$ between 10^{-4} and 0.2, which lies in the range expected for large planet-building impacts. In (b), iSALE simulations at M = 3 and M = 6 are shown using the same colors as the corresponding scalings at these Mach values (plain curves).

8 Conclusion

In this study, we explore how more accurately impact experiments in water at subsonic velocity can be usedto describe the dynamics of planetary-scale impacts during planetary formation. Combining numerical modelling of impacts and laboratory water impact experiments, we investigate the transition from subsonic to supersonic collisions onto a liquid target. The use of iSALE, initially developed and benchmarked for hypervelocity physics (e.g., Amsden et al., 1980; Collins et al., 2002; Wünnemann et al., 2005; Güldemeister et al., 2013; Kowitz et al., 2013), has been validated against experiments at subsonic conditions. We then use iSALE simulations to analyse the transition between subsonic and hypersonic collisions by systematically varying the Froude and Mach numbers as two independent parameters. We show that different materials with different equations of state assuming hydrodynamic behavior, exhibit approximately the same maximum crater depth scaling as a function of the Mach number. In the supersonic regime (M > 1), the normalised crater depth decreases with increasing Mach number. The numerical results for the maximum crater depth are fitted with a scaling law that depends on both the Froude and Mach numbers, as deduced from the energy balance argument following Miranda and Dowling (2019). Our best-fit scaling agrees well with experimental and numerical data over four orders of magnitude in Mach number within the range of Froude num-

bers expected for planet-building collisions. The scaling we propose here applies to the gravity regime of crater formation, i.e. when the cohesive strength of the material is negligible and hydrodynamic behavior can be assumed. Our scaling suggests a dependence of the cratering process on the Mach number that was previously neglected in the formalism of the π-group scaling (e.g., K. Holsapple & Schmidt, 1982; K. A. Holsapple, 1993) but was recognized to affect crater formation in granular materials (Miranda & Dowling, 2019). In particular, our scaling explains the remarkable extrapolation over orders of magnitude in Froude number between hypervelocity experiments and subsonic experiments (K. Holsapple & Schmidt, 1982). This extrapolation is reasonably accurate for Mach numbers smaller than 3. For larger Mach numbers, the π-group scaling deviates from the data by more than 20%. The change in crater depth scaling from subsonic to supersonic impacts results from a difference in the energy partitioning with more energy going into the shock wave generation and propagation in the hypervelocity case. In addition, our scaling law suggests that the maximum crater depth is limited by the ratio of the sound speed squared to the impactor weight for very large Mach numbers. In this regime, an increase in the impact kinetic energy does not cause an increase in the crater size because a large fraction of the incoming energy is transferred into internal energy in the target material. The energy and momentum transfer upon impact from subsonic to hypersonic regimes have to be further explored. In particular the distribution of internal energy into compression and heating requires further investigation.

Our results additionally suggest that the current understanding on crater formation on Mars, Earth, the Moon and Mercury may be revised. In particular, estimates of the impactor sizes to form a given crater observed on a planetary surface may deviate from previous assumptions based on scaling laws where the effect of the Mach number was not taken into account. The significance increases for sufficiently large Mach numbers. For instance, the average velocity on Mars is about 10 km.s^{-1} (e.g., Ivanov, 2001), which correspond roughly to a Mach number of 2.24 if Mars surface is assumed to be basaltic. In this case, figure 9 suggests that the Froude number would have to be superior to ~ 1000 to predict an accurate (within a few percents) impactor size with the π-group scaling. This means that for any impactor projectile larger than ~ 25 km in radius, the projectile size would be under-estimated by the π-group scaling. In the case of Mercury, for which the average impact velocities are estimated to be between 17 km.s^{-1} (Borin et al., 2009) and 20.5 km.s^{-1} (Cintala, 1992), corresponding to Mach numbers

in between 3.8 and 4.6, the sizes of the projectiles would have to be smaller than 4 km for the π-group scaling. For example, for an impact on Mars with a Froude number of 500, at a speed of about 10km.s^{-1}, the error on the relative crater size estimate would be of about 10%. Finally, previous studies have shown that the cratering process affects the mixing between the impactor core and the target silicates (Landeau et al., 2021; Lherm et al., 2022). As we find that the Mach number affects the excavation of the crater, our results suggest that the Mach number might also affect the mixing. This will be investigated in a follow-up study.

Open Research Section

Numerical simulations are produced with the iSALE-2D shock physics code (https://isale-code.github.io/). In particular, we use the iSALE-2D Dellen release of the iSALE shock physics code (Amsden et al., 1980; Collins et al., 2004; Wünnemann et al., 2006). The iSALE-2D Dellen release is distributed on a case-by-case basis to academic users in the impact community, strictly for non-commercial use. Scientists interested in using or developing iSALE may apply to use iSALE at https://isale-code.github.io/access.html. Data are further processed with python 2.7. Figures were made with Matplotlib version 3.2.1 (Caswell et al., 2020; Hunter, 2007). Some plots in this work were created with the pySALE-Plot tool written by Tom Davison. All data to produce the figures and the iSALE input files in this work can be accessed in this document, in table 2 and table 3 for the simulations and in the appendix A1 for the experiments.

Acknowledgement

References

Amsden, A., Ruppel, H., & Hirt, C. (1980). *Sale: A simplified ale computer program for fluid flow at all speeds* (Tech. Rep.). Los Alamos Scientific Lab., NM (USA).

Badro, J., Siebert, J., & Nimmo, F. (2016). An early geodynamo driven by exsolution of mantle components from earth's core. *Nature*, *536*(7616), 326–328.

Bisighini, A., Cossali, G. E., Tropea, C., & Roisman, I. V. (2010). Crater evolution after the impact of a drop onto a semi-infinite liquid target. *Physical Review E*, *82*(3), 036319.

Borin, P., Cremonese, G., Marzari, F., Bruno, M., & Marchi, S. (2009). Statistical analysis of micrometeoroids flux on mercury. *Astronomy & Astrophysics*, *503*(1), 259–264.

Caswell, T. A., Droettboom, M., Lee, A., Hunter, J., Firing, E., Sales De Andrade, E., ... others (2020). matplotlib/matplotlib: Rel: v3. 3.1. *Zenodo*.

Chambers, J. E. (2004). Planetary accretion in the inner solar system. *Earth and Planetary Science Letters*, *223*(3-4), 241–252.

Cintala, M. J. (1992). Impact-induced thermal effects in the lunar and mercurian regoliths. *Journal of Geophysical Research: Planets*, *97*(E1), 947–973.

Collins, G. S., Melosh, H. J., & Ivanov, B. A. (2004). Modeling damage and deformation in impact simulations. *Meteoritics & Planetary Science*, *39*(2), 217–231.

Collins, G. S., Melosh, H. J., Morgan, J. V., & Warner, M. R. (2002). Hydrocode simulations of chicxulub crater collapse and peak-ring formation. *Icarus*, *157*(1), 24–33.

Deguen, R., Landeau, M., & Olson, P. (2014). Turbulent metal–silicate mixing, fragmentation, and equilibration in magma oceans. *Earth and Planetary Science Letters*, *391*, 274–287.

Elbeshausen, D., Wünnemann, K., & Collins, G. S. (2009). Scaling of oblique impacts in frictional targets: Implications for crater size and formation mechanisms. *Icarus*, *204*(2), 716–731.

Elkins-Tanton, L. T. (2012). Magma oceans in the inner solar system. *Annual Review of Earth and Planetary Sciences*, *40*, 113–139.

Engel, O. G. (1967). Initial pressure, initial flow velocity, and the time dependence of crater depth in fluid impacts. *Journal of applied physics*, *38*(10), 3935–3940.

Gault, D. E., Quaide, W. L., & Oberbeck, V. R. (1974). Impact cratering mechanics and structures. *A primer in lunar geology*, 177–189.

Gault, D. E., & Sonett, C. P. (1982). Laboratory simulation of pelagic asteroidal impact: Atmospheric injection, benthic topography, and the surface wave radiation field.

Güldemeister, N., Wünnemann, K., Durr, N., & Hiermaier, S. (2013). Propagation of impact-induced shock waves in porous sandstone using mesoscale modeling. *Meteoritics & Planetary Science*, *48*(1), 115–133.

Güldemeister, N., Wünnemann, K., & Poelchau, M. (2015). Scaling impact crater dimensions in cohesive rock by numerical modeling and laboratory experi-

ments. *Geological Society of America Special Papers*, *518*, 17–29.

Holsapple, K., & Schmidt, R. (1980). On the scaling of crater dimensions: 1. explosive processes. *Journal of Geophysical Research: Solid Earth*, *85*(B12), 7247–7256.

Holsapple, K., & Schmidt, R. (1982). On the scaling of crater dimensions: 2. impact processes. *Journal of Geophysical Research: Solid Earth*, *87*(B3), 1849–1870.

Holsapple, K. A. (1993). The scaling of impact processes in planetary sciences. *Annual review of earth and planetary sciences*, *21*, 333–373.

Housen, K., Schmidt, R., & Holsapple, K. (1983). Crater ejecta scaling laws: Fundamental forms based on dimensional analysis. *Journal of Geophysical Research: Solid Earth*, *88*(B3), 2485–2499.

Housen, K. R., & Holsapple, K. A. (2003). Impact cratering on porous asteroids. *Icarus*, *163*(1), 102–119.

Housen, K. R., & Holsapple, K. A. (2011). Ejecta from impact craters. *Icarus*, *211*(1), 856–875.

Housen, K. R., Sweet, W. J., & Holsapple, K. A. (2018). Impacts into porous asteroids. *Icarus*, *300*, 72–96.

Hunter, J. D. (2007). Matplotlib: A 2d graphics environment. *Computing in science & engineering*, *9*(03), 90–95.

Hyodo, R., & Genda, H. (2020). Escape and accretion by cratering impacts: Formulation of scaling relations for high-speed ejecta. *The Astrophysical Journal*, *898*(1), 30.

Ichikawa, H., Labrosse, S., & Kurita, K. (2010). Direct numerical simulation of an iron rain in the magma ocean. *Journal of Geophysical Research: Solid Earth*, *115*(B1).

Ivanov, B. A. (2001). Mars/moon cratering rate ratio estimates. *Space Science Reviews*, *96*(1-4), 87–104.

Kendall, J. D., & Melosh, H. (2016). Differentiated planetesimal impacts into a terrestrial magma ocean: Fate of the iron core. *Earth and Planetary Science Letters*, *448*, 24–33.

Kowitz, A., Güldemeister, N., Reimold, W., Schmitt, R., & Wünnemann, K. (2013). Diaplectic quartz glass and sio2 melt experimentally generated at only 5 gpa shock pressure in porous sandstone: Laboratory observations and meso-scale numerical modeling. *Earth and Planetary Science Letters*, *384*, 17–26.

Landeau, M., Deguen, R., Phillips, D., Neufeld, J. A., Lherm, V., & Dalziel, S. B. (2021). Metal-silicate mixing by large earth-forming impacts. *Earth and Planetary Science Letters*, *564*, 116888.

Lherm, V., & Deguen, R. (2018). Small-scale metal/silicate equilibration during core formation: The influence of stretching enhanced diffusion on mixing. *Journal of Geophysical Research: Solid Earth*, *123*(12), 10–496.

Lherm, V., Deguen, R., Alboussière, T., & Landeau, M. (2022). Rayleigh–taylor instability in impact cratering experiments. *Journal of Fluid Mechanics*, *937*, A20.

Manske, L., Marchi, S., Plesa, A.-C., & Wünnemann, K. (2021). Impact melting upon basin formation on early mars. *Icarus*, *357*, 114128.

Melosh, H. J. (1989). Impact cratering: A geologic process. *New York: Oxford University Press; Oxford: Clarendon Press*.

Miranda, C. S., & Dowling, D. R. (2019). Mach number scaling of impact craters in unconsolidated granular materials. *Icarus*, *325*, 84–93.

Monteux, J., & Arkani-Hamed, J. (2014). Consequences of giant impacts in early mars: core merging and martian dynamo evolution. *Journal of Geophysical Research: Planets*, *119*(3), 480–505.

Nakajima, M., Golabek, G. J., Wünnemann, K., Rubie, D. C., Burger, C., Melosh, H. J., . . . Hull, S. D. (2021). Scaling laws for the geometry of an impact-induced magma ocean. *Earth and Planetary Science Letters*, *568*, 116983.

O'Keefe, J. D., & Ahrens, T. J. (1993). Planetary cratering mechanics. *Journal of Geophysical Research: Planets*, *98*(E9), 17011–17028.

O'Rourke, J. G., & Stevenson, D. J. (2016). Powering earth's dynamo with magnesium precipitation from the core. *Nature*, *529*(7586), 387–389.

Pumphrey, H. C., & Elmore, P. A. (1990). The entrainment of bubbles by drop impacts. *Journal of Fluid Mechanics*, *220*, 539–567.

Qaddah, B., Monteux, J., Clesi, V., Bouhifd, M. A., & Le Bars, M. (2019). Dynamics and stability of an iron drop falling in a magma ocean. *Physics of the Earth and Planetary Interiors*, *289*, 75–89.

Ray, B., Biswas, G., & Sharma, A. (2015). Regimes during liquid drop impact on a liquid pool. *Journal of Fluid Mechanics*, *768*, 492–523.

Raymond, S. N., O'Brien, D. P., Morbidelli, A., & Kaib, N. A. (2009). Building the terrestrial planets: constrained accretion in the inner solar system. *Icarus*, *203*(2), 644–662.

Rubie, D., Melosh, H., Reid, J., Liebske, C., & Righter, K. (2003). Mechanisms of metal–silicate equilibration in the terrestrial magma ocean. *Earth and Planetary Science Letters*, *205*(3-4), 239–255.

Samuel, H. (2012). A re-evaluation of metal diapir breakup and equilibration in terrestrial magma oceans. *Earth and Planetary Science Letters*, *313*, 105–114.

Santini, M., Fest-Santini, S., & Cossali, G. (2017). Experimental study of vortices and cavities from single and double drop impacts onto deep pools. *European Journal of Mechanics-B/Fluids*, *62*, 21–31.

Schmidt, R. (1977). A centrifuge cratering experiment-development of a gravity-scaled yield parameter. In *Impact and explosion cratering: Planetary and terrestrial implications* (pp. 1261–1278).

Schmidt, R. (1980). Meteor crater: Energy of formation-implications of centrifuge scaling. In *Lunar and planetary science conference proceedings* (Vol. 11, pp. 2099–2128).

Schmidt, R., & Housen, K. (1987). Some recent advances in the scaling of impact and explosion cratering. *International Journal of Impact Engineering*, *5*(1-4), 543–560.

Tillotson, J. H. (1962). *Metallic equations of state for hypervelocity impact* (Tech. Rep.). General Dynamics San Diego CA General Atomic DIV.

Tonks, W. B., & Melosh, H. J. (1993). Magma ocean formation due to giant impacts. *Journal of Geophysical Research: Planets*, *98*(E3), 5319–5333.

Ulvrová, M., Coltice, N., Ricard, Y., Labrosse, S., Dubuffet, F., Velímský, J., & Šrámek, O. (2011). Compositional and thermal equilibration of particles, drops, and diapirs in geophysical flows. *Geochemistry, Geophysics, Geosystems*, *12*(10).

Walsh, K. J., Morbidelli, A., Raymond, S. N., O'Brien, D. P., & Mandell, A. M. (2011). A low mass for mars from jupiter's early gas-driven migration. *Nature*, *475*(7355), 206.

Wetherill, G. (1996). The formation and habitability of extra-solar planets. *Icarus*, *119*(1), 219–238.

Wünnemann, K., Collins, G., & Melosh, H. (2006). A strain-based porosity model for use in hydrocode simulations of impacts and implications for transient crater growth in porous targets. *Icarus*, *180*(2), 514–527.

Wünnemann, K., Morgan, J., & Jödicke, H. (2005). Is ries crater typical for its size? an analysis based upon old and new geophysical data and numerical modeling. *Large meteorite impacts III*, *384*, 67–83.

Appendix A Details on the two explored experiments

For both E1 and E2, the experimental setup is the following:

- The balloon is tied to a string, itself attached to the frame, so that the balloon latex membrane does not fall into the target and hence, it does not affect the cratering process.

- The density of the target and impacting liquid is 998.66kg m^3.

- We record the flow with a Photron SA1.1 monochrome high-velocity camera with a resolution of 1024×1024pixels and at a frame rate of 2000 frames per second. The camera is placed at a horizontal distance of 2 m from the tank and at a height of 1.4 m from the floor.

- We illuminate the tank from the back with a panel of red LEDs, which measures 90cm $\times$120cm. To obtain a uniform light source, we place a diffusive screen between the panel and the tank. The length scale in experimental images is callibrated using a panel containing vertical and horizontal lines of dots spaced by 2 cm.

- Before each experiment, we compute the spherical radius R of the impactor from the weight of the balloon and the density of the impacting liquid. We also compute the impact velocity U and the crater depth from the experimental images using routines written in python. We first subtract the backfield image to each frame. We then select a constant pixel intensity threshold below which the pixel intensity is set to 0 to remove the backfield noise. From each frame before the impactor reaches the target, we locate the 2D centroid of the impactor. We fit the position of this centroid as a function of time with a quadratic polynomial. From this fit, we compute the velocity U at the time when the front of the impacting liquid first touches the water target. From each frame after the impactor reaches the target, we automatically detect the position of the crater floor and we extract the crater depth Z_c. Uncertainties on U and Z_c are typically on the order of 5%.

E1 and E2 parameters, as well as the associated dimensionless numbers are summarized in table A1.

Table A1. Parameter values in experiments E1 and E2 with no density difference. With U the impact speed, U_s the sound velocity in the medium, g the gravitational acceleration, R the impact radius, ν_t, ν_i and ν_a the target, impactor and air kinematic viscosity respectively, ρ_t, ρ_i and ρ_a the respective densities of the target, the impactor and air, σ_t, and σ_i, the respective target and impactor surface tensions, L the target width and H_t the target depth. The frame rate is 2000 frames per second in both movies from which data are then exploited.

Dimensionless number	Experiment E1	Experiment E2
$U(meter/second)$	1.35 ± 0.1	5.3 ± 0.3
$U_s(meter/second)$	1481.0	1481.0
$R(meter)$	0.0305 ± 0.00005	0.0308 ± 0.00005
$g \ (\mathrm{m\,s^{-2}})$	9.81	9.81
$Fr = \frac{U^2}{g\,R}$	6 ± 1	93 ± 10
$M = \frac{U}{U_s}$	$9 \times 10^{-4} \pm 5 \times 10^{-5}$	$3.6 \times 10^{-3} \pm 10^{-4}$
$Re = \frac{U\,R}{\nu_t}$	$4.1 \times 10^4 \pm 3 \times 10^3$	$1.6 \times 10^5 \pm 10^4$
$We = \frac{\rho_t U^2 R}{\sigma_t}$	760 ± 100	$1.2 \times 10^4 \pm 10^3$
$P = \frac{\rho_i - \rho_t}{\rho_t}$	0	0
ρ_t/ρ_a	830	830
ν_i/ν_t	1	1
ν_t/ν_a	0.0660	0.0660
σ_i/σ_t	1	1
L/R	25	25
H_t/R	16	16

Appendix B Crater diameter estimates

Among the extensive studies on cratering processes, the transient crater diameter is more studied as the crater depth itself. Thus, here, results for the crater diameter are also produced. In this case, to better compare with the π-group scaling (given for the

777   transient crater diameter), we take the crater diameter when the maximum crater depth

778   is reached. Results are shown in figure. B1 and figure. B2.

779   The figure. B1 is the equivalent for crater diameter of the figure. 6 previously given

780   for the crater depth. It is visible that the data are sparser. That is due to the compli-

781   cated estimates of the transient crater size within the simulations, notably for the higher

782   impact velocities. However, the results overall show the same general trend as a func-

783   tion of M as does the maximum crater depth. No good fit of the data could be produced

784   in that case. We also compare our results to the pi-group scaling predictions in figure. B2.
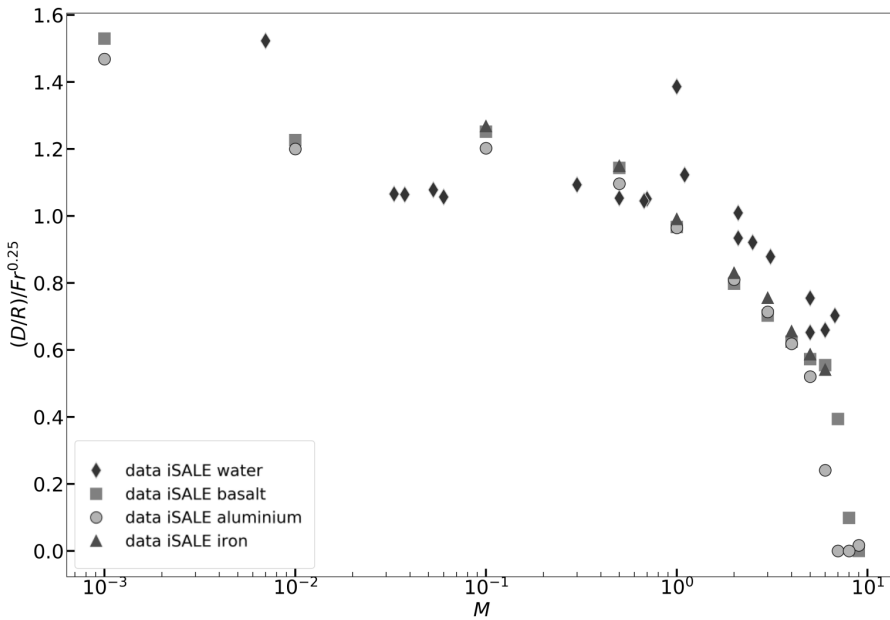
Figure B1.   Crater diameter D, measured at the time when the maximum crater depth is reached, normalised by $RFr^0.25$, as a function of the Mach number M.

Appendix C   Energy partitioning estimates: iSALE post-processing

786   The impactor kinetic energy is simply calculated as $E_k^{imp} = \frac{1}{2}m_i U^2$. Then, for

787   each timestep, the total kinetic energy in the target is estimated. To do so, the kinetic

788   energy contained in each grid-cell is computed with $E_k^{cell} = \frac{1}{2}m_{cell}v_{cell}^2$, with m_{cell} the

789   mass contained in one cell and v_{cell} the particle velocity in the cell. The mass contained

790   in a given cell depends on the material density in the cell ρ_{cell}, which is affected by the

791   shock, and the cell volume V_{cell}. The volume of each grid-cell is estimated beforehand

792   by estimating the volume of a ring, according the the cylindrical geometry of the grid

793   used here. The density depends on the depth and on the shock wave propagation and
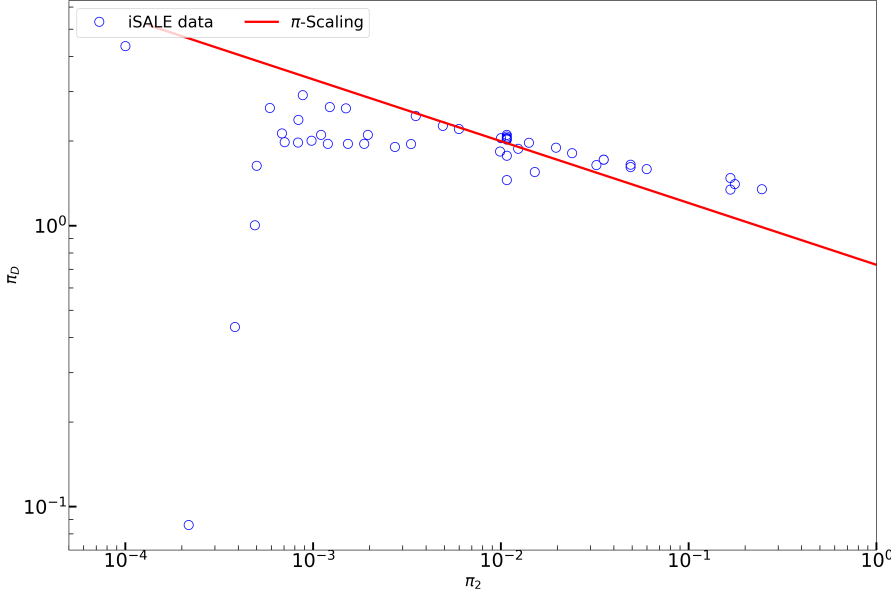
Figure B2. pi-D as a function of pi-2 for our numerical simulations results. The pi-group scaling is plotted as the red line.

thus evolves with both space and time during the simulation. The fraction of impactor to target material in each cell is also tracked by iSALE and stored in the data file that is post-processed. Accordingly, it is possible to deduce which kinetic energy contained in the cell belongs to impactor material or to target material. Both are tracked independently from one another and are estimated from the respective masses of the material in each cell $m_{mat} = \rho_{cell} V_{cell} f_{mat}$ with m_{mat} the mass of the material mat (impactor or target) in the cell and f_{mat} the mass fraction of that given material that is contained in the cell. The total kinetic energy transferred into the target is then estimated by summing over all cells the target kinetic energy contained in each of these. The procedure is similar for the kinetic energy remaining in the impactor material. iSALE also computes the specific internal energy within each cell. Initially, the target already contains a given amount of specific internal energy. To make sure that what we estimate is only resulting from the impact itself, we correct the specific internal energy of each cell (and for every timestep) by its initial value. This has to be translated into internal energy by multiplying it to the cell mass, after what the contribution of each independent cell is considered by summing over all of them. The required additional energy to ensure conservation of energy is assumed to be gravitational potential energy (it should result from both the crater opening and the ejecta).